Large Spin Anomalous Hall Effect in $L1_0$-FePt:

Symmetry and Magnetization Switching

Takeshi Seki[1,2,*], Satoshi Iihama[3], Tomohiro Taniguchi[4], and Koki Takanashi[1,2]

1 Institute for Materials Research, Tohoku University, Sendai 980-8577, Japan

2 Center for Spintronics Research Network, Tohoku University, Sendai 980-8577, Japan

3 WPI Advanced Institute for Materials Research, Tohoku University, Sendai 980-8577, Japan

4 National Institute of Advanced Industrial Science and Technology (AIST), Spintronics Research Center, Tsukuba, 305-8568, Japan

*Author to whom correspondence should be addressed.

Electronic mail: go-sai@imr.tohoku.ac.jp

Abstract

We quantitatively evaluate a spin anomalous Hall effect (SAHE), generating spin angular momentum flow (spin current, J_s), in an $L1_0$-FePt ferromagnet by exploiting giant magnetoresistance devices with $L1_0$-FePt / Cu / $Ni_{81}Fe_{19}$. From the ferromagnetic resonance linewidth modulated by the charge current (J_c) injection, the spin anomalous Hall angle (α_{SAH}) is obtained to be 0.25 ± 0.03. The evaluation of α_{SAH} at different configurations between J_c and magnetization enables us to discuss the symmetry of SAHE and gives the unambiguous evidence that SAHE is the source of J_s. Thanks to the large α_{SAH}, we demonstrate the SAHE-induced magnetization switching.

(99 words)

High efficient conversion from J_c to J_s and vice versa is the key for spintronics to enhance

device performance and to provide with multi-functionality. The most promising way to convert from

J_c to J_s is to exploit spin Hall effect (SHE) [Refs. 1, 2]. SHE is a relativistic effect expressed as

$$\mathbf{J}_s = (\hbar/2e)\alpha_{SH}[\hat{\sigma} \times \mathbf{J}_c], \qquad (1)$$

where α_{SH} is the spin Hall angle, e (< 0) is the electric charge of an electron and $\hat{\sigma}$ is the

quantization axis of electron spin. The experimental studies on SHE have first been done in

nonmagnetic semiconductors [Refs. 3,4] followed by nonmagnetic metals with large spin orbit

coupling parameters [Ref. 5]. As in SHE of nonmagnets (NM), one can expect the charge-spin

conversion in a ferromagnet (FM). In the first stage, the conversion from J_s to J_c in FM was reported

[Refs. 6-8], followed by the theory of spin anomalous Hall effect (SAHE) [Ref. 9] and experiments

generating J_s [Refs. 10-13]. The most apparent difference between SHE in NM and SAHE in FM is

that the charge current appears in the transverse direction due to the anomalous Hall effect (AHE) [Ref.

14], J_c^{AHE}, which is defined as

$$\mathbf{J}_c^{AHE} = \alpha_{AH}[\hat{p} \times \mathbf{J}_c], \qquad (2)$$

where α_{AH} is the anomalous Hall angle and $\hat{p}$ is the quantization axis of local spin in FM. This

transverse J_c^{AHE} is spin-polarized by the factor of ζ that refers to the polarization of AHE [Ref. 9].

Although this J_c^{AHE} gives rise to $-J_c^{AHE}$ in the open circuit condition, $-J_c^{AHE}$ is spin-polarized by the

factor of β representing the spin polarization factor in the longitudinal J_c flow. Consequently, J_s

originating from SAHE can be written as [Ref. 9]

$$\mathbf{J}_s^{SAHE} = (\hbar/2e)(\zeta - \beta)\alpha_{AH}[\hat{p} \times \mathbf{J}_c], \qquad (3)$$

where $(\zeta - \beta)\alpha_{AH}$ corresponds to spin anomalous Hall angle (α_{SAH}). Equation (3) means that J_s^{SAHE}

depends on $\hat{p}$, $i.e.$ $\mathbf{M}$. If $\hat{p}$ // $\mathbf{J}_c$, J_s^{SAHE} becomes zero. In contrast to the reports on SAHE [Refs.

10-14], the recent studies found the various phenomena different from SAHE such as SHE [Ref. 15] and an interface scattering effect [Refs. 16,17]. Therefore, the identification of SAHE requires the elimination of these other effects. Another important issue confronted with SAHE is its low conversion efficiency. Since SAHE has benefits that SHE does not have, *e.g.* the ability of reorientation of antidamping torque along $\hat{p}$ and resultant zero-field magnetization switching [Ref. 9], a FM exhibiting large α_{SAH} is first essential for practical applications.

In this study, we focus on a ferromagnetic metal $L1_0$-FePt because large AHE has been reported for $L1_0$-FePt [Ref. 18]. In order to evaluate α_{SAH} quantitatively, we carried out the ferromagnetic resonance (FMR) measurement for the giant magnetoresistance (GMR) device composed of $L1_0$-FePt (d^{FePt} = 30 nm) | Cu (3 nm) | $Ni_{81}Fe_{19}$ (Permalloy: Py, d^{Py} =2 nm), in which the $L1_0$-FePt has the in-plane uniaxial magnetic anisotropy. **Fig. 1** depicts the concept of the present experiment and the measurement configurations. The application of dc current (corresponding to J_c) flowing in the $L1_0$-FePt layer is converted into J_s^{SAHE}, and J_s^{SAHE} interacts with M of Py (its unit vector is defined as **m**), resulting in the modification of FMR linewidth due to the enhanced or reduced magnetization damping of Py. A key of this study is that the strong in-plane uniaxial magnetic anisotropy of $L1_0$-FePt enables us to utilize two different relative configurations between J_c and M of FePt (its unit vector is defined as **p**). As shown in **Fig. 1(a)**, the orthogonal configuration of $\mathbf{J}_c \perp \mathbf{p}$ corresponds to the evaluation of SAHE. Other possible effects such as SHE and interface effect can be identified in the parallel configuration of $\mathbf{J}_c // \mathbf{p}$. We fabricated the rectangular-shaped devices with the orthogonal and parallel configurations on the identical substrate (**Figs. 1(b) and 1(c)**). Together with dc current (I_{dc}), the radiofrequency current (I_{rf}) was applied to generate an oscillating magnetic field, which excited FMR in the Py. The length of GMR device was fixed at 10 μm while the width (w) of

device was varied: $w = 1$ μm or 4 μm.

The thin films were grown on an SrTiO₃ (110) single crystal substrate with the stack of SrTiO₃ subs. ‖ FePt (30) | Cu (2) | Py (3) | Al-O (10) (in nanometer). All the layers except FePt were grown at ambient temperature. The FePt (110) layer was epitaxially grown on the SrTiO₃ substrate using an ultrahigh vacuum magnetron sputtering system at 450 ℃. After the FePt deposition, the sample was transferred to the ion beam sputtering (IBS) chamber. After cleaning the FePt surface by soft Ar ion milling, the Cu | Py | Al-O layers were deposited on the FePt employing the IBS. The film structure was characterized using the x-ray diffraction (XRD) with Cu-$K\alpha$ radiation. The alloy compositions of FePt and Py were determined to be $Fe_{54}Pt_{46}$ and $Ni_{81}Fe_{19}$, respectively, by electron probe x-ray microanalysis. Magnetization was measured at room temperature using the vibrating sample magnetometer. The thin films were patterned into the rectangular shapes through the use of electron beam lithography and Ar ion milling. Finally, the Au | Cr contact pads with the co-planar waveguide (CPW) shape were formed. For the FMR measurement, the rf power of 5 dBm with a fixed f_0 was applied to the signal line of CPW from a signal generator, which induced the transverse rf magnetic field. When the FMR condition of Py was satisfied with sweeping H_{ext}, the device resistance ($R(t)$) oscillated through the GMR effect. As a result, the applied $I_{rf}(t)$ ($= I \cos(2\pi f_0 t)$) and the oscillating $R(t)$ ($\propto \cos(2\pi f_0 t)$) generated the rectification dc voltage (V_{dc}), which was detected by the lock-in amplifier. For the FMR measurement with the I_{dc} application, the sourcemeter was connected to the dc port of bias-T.

Let us first explain the structure and the magnetic properties of GMR tri-layer. The out-of-plane x-ray diffraction profile (**Fig. 2(a)**) shows only the 220 diffractions of FePt, Cu and Py while in the in-plane XRD (**Fig. 2(b)**) only the 00l diffractions of FePt, Cu and Py are observed. The in-plane ϕ scan for FePt 200 diffraction (**Fig. 2(c)**) exhibits the two-fold rotational symmetry.

Therefore, the GMR tri-layer was grown with the epitaxial relationship of $(110)_{SrTiO3}$ || $(110)_{FePt}$ || $(110)_{Cu}$ || $(110)_{Py}$, $[001]_{SrTiO3}$ || $[001]_{FePt}$ || $[001]_{Cu}$ || $[001]_{Py}$. In addition, the appearance of FePt 001 and 003 superlattice peaks in **Fig. 2(b)** indicates that $L1_0$-ordered FePt was formed. The crystal orientation relationship between $SrTiO_3$ and $L1_0$-FePt is schematically shown in **Fig. 2(d)**. **Fig. 2(e)** represents the magnetization curves with H_{ext} applied along the in-plane [001] and $[1\bar{1}0]$ directions and the out-of-plane [110] direction. It is obvious that the $L1_0$-FePt layer has the strong in-plane uniaxial magnetic anisotropy along the in-plane [001] direction. As in the case of $L1_0$-FePt layer, the Py also exhibits the non-negligible in-plane magnetic anisotropy along the [001]. The two-step behavior of magnetization switching is observed in the in-plane [001] magnetization curve, indicating the induction of coercivity difference between $L1_0$-FePt and Py.

Fig. 3(a) shows the current-in-plane (CIP) GMR curves for the orthogonal configuration-device with w = 4 μm at the magnetic field angles (θ_H), defined in **Fig. 1(b)**, of 0°, 15°, and 90°. The detailed θ_H dependence of MR curve for the orthogonal and parallel configuration-devices are given in **Supplemental Materials** [Ref. 19]. The orthogonal configuration was achieved for θ_H = 0° by increasing H_{ext}. On the other hand, the full GMR curve was obtained when H_{ext} was swept at θ_H = 90°. These MR curves indicate that **m** is easily aligned along $\mathbf{H}_{ext}$ while **p** acts as a fixed polarizer, resulting in the orthogonal configuration at small θ_H. **Figs. 3(b) and 3(c)** show the FMR spectra for the orthogonal configuration-device at I_{dc} = 4 mA and -4 mA, respectively. θ_H was set at -10° and f_0 was 4 GHz. V_{dc} was generated by the rectification effect through the CIP-GMR effect, and the resonance peak comes from the FMR of Py. The experimental spectra were fitted by the Lorentzian and anti-Lorentzian functions together with the linear background for taking into account the slight change in the device resistance with H_{ext} (see [Ref. 19] for details of fitting). One can see the clear variation in the spectral linewidth (ΔH_{Res}) between I_{dc} = 4 mA and -4 mA. The

ΔH_{Res} versus I_{dc} for θ_{H} = -10° and +15° is plotted in **Figs. 3(d) and 3(e)**, respectively. The linear

variations are observed, and it slope depends on θ_{H}. It is noted that the odd-functional behavior of

ΔH_{Res} against I_{dc} is not explained by the spin transfer torque (STT) of GMR stack because the sign of

STT, *i.e.* damping or anti-damping, in the CIP-GMR device is not determined by the I_{dc} direction. **Fig.**

3(f) summarizes the modulation linewidth, $d\Delta H_{\text{Res}}$ / dI_{dc}, as a function of θ_{H} for the orthogonal

configuration-device. The experimental data were well fitted by the following equation:

$$\frac{d\Delta H_{\text{Res}}}{dI_{\text{dc}}} = \alpha_{\text{SAH}} \frac{\hbar}{e} \left(\frac{C^{\text{FePt}}}{wd^{\text{FePt}}} \right) \cdot \left(\frac{2\pi f_0}{\gamma \cos\left(\varphi^{\text{Py}} - \theta_{\text{H}}\right)} \right) \cdot \left(\frac{\sin\varphi^{\text{Py}}}{\mu_0 M_{\text{S}}^{\text{Py}} d^{\text{Py}} \left(H_{\text{XX}} + H_{\text{YY}}\right)} \right), \quad (4)$$

where C^{FePt} is the shunt ratio of the current flowing in the $L1_0$-FePt layer to the total I_{dc}, γ is the

gyromagnetic ratio, φ^{Py} is the angle of **m** respective to $\mathbf{J}_{\text{c}}$, M_{s}^{Py} is the saturation magnetization of Py,

$H_{\text{XX(YY)}}$ represents the in-plane (out-of-plane) effective field for Py (see [Ref. 19] for the derivation of

Eq. (4)). We assumed that **p** is pinned along the direction orthogonal to $\mathbf{J}_{\text{c}}$. The values of γ, φ^{Py}, M_{s}^{Py}

and $H_{\text{XX(YY)}}$ were determined by the θ_{H} dependence of FMR spectra without I_{dc} application, and C^{FePt} =

0.315 was calculated considering the parallel circuit (see [Ref. 19]). As a result, α_{SAH} for the

orthogonal configuration-device was obtained to be 0.25 ± 0.03. Let us discuss the magnitude of α_{SAH}

here. This α_{SAH} is significantly larger than - 0.14 ± 0.05 for CoFeB [Ref. 12]. As described above,

α_{SAH} is given by $(\zeta - \beta)\alpha_{\text{AH}}$. α_{AH} of FePt was evaluated to be 0.03 by measuring AHE (see [Ref.

19]). The previous transport experiments using $L1_0$-FePt suggest $\beta \sim 0.4$ at most [Ref. 20]. This means

that large ζ = 8.7 is required in order to explain the large α_{SAH}. We note that the parameter ζ is defined

as a ratio of the spin current to the transverse charge current by AHE. Therefore, if the spin-up and

spin-down electrons are scattered to the opposite direction, ζ can be larger than one. The parameter ζ

was introduced in Ref. 9 phenomenologically, and an evaluation of its value by, for example,

first-principles calculation has not been reported yet. Our result, however, suggests that even a FM

with a small AHE (α_{AH}) has a possibility to be a high-efficient J_s source by SAHE.

As mentioned above, several origins of J_s, other than SAHE, have been proposed in CIP-GMR structures. For example, the inverse SHE of Co was reported in Co | Cu | $Y_3Fe_5O_{12}$ [Ref. 14], where the spin polarization is geometrically determined and is independent from **M**. We confirm that such M-independent SHE does not exist in our sample by measuring the FMR in the parallel configuration. Note that SAHE becomes zero in the parallel configuration whereas the M-independent SHE is finite if exists. However, no clear θ_H dependence of dΔH_{Res} / dI_{dc} was seen for the parallel configuration-device (**Fig. 3(g)**, the FMR spectra are given in [Ref. 19]), indicating that the M-independent SHE is negligible in our experiment. Another possible source of J_s is the interface scattering effect [Ref. 16]. Recently, the interface-induced spin orbit torque has also been observed in Py (or CoFeB) | Ti | CoFeB [Ref. 17]. J_s generated by the interface scattering effect provides two kinds of spin torques. One has the spin polarization identical to that of the M-independent SHE, and therefore, is negligible due to the same reason explained above. The other has the polarization along the direction perpendicular to the film plane, as in the case of the previous work [Ref. 17]. We note that the average of this torque over the precession of **m** becomes zero. Therefore, this torque does not affect ΔH_{Res}. In summary, several phenomena of J_s generation reported in the previous works are negligibly small or do not affect our measurement, and we can conclude that the modulation of ΔH_{Res} is solely due to the SAHE.

Let us move to the magnetization switching experiment. We characterized the static magneto-transport properties under the I_{dc} application for the orthogonal configuration-device with w = 1 μm. The minor GMR curves at I_{dc} = 0 mA and ± 4.8 mA are shown in **Figs. 4(a) and 4(b)**, respectively, where θ_H was set at 60º in order to increase the projection component of **m** to **p**. This projection component is inevitable for the deterministic switching. On the other hand, this θ_H led to the

partial (not full) magnetization switching of Py. The remarkable loop shift was observed by applying I_{dc}, which is attributable to the SAH torque. The switching experiment was carried out using the measurement sequence schematically shown in **Fig. 4(c)**. **Fig. 4(d)** demonstrates that the I_{dc} application can switch the magnetization direction of Py. This switching behavior is similar to conventional spin orbit torque switching using nonmagnetic materials [Refs. 21-23] and topological insulators [Refs. 24,25]. The current density (J) for switching is shifted with H_{ext}. We achieved the small switching current of $|J| < 10^7$ A/cm^2 at $H_{ext} = 325$ Oe. This value is consistent with the small critical switching current density of $\sim 3.1 \times 10^6$ A/cm^2 estimated theoretically with the experimental α_{SAH} (see [Ref. 19]). We also examined the current-induced switching at the condition where **p** has the opposite polarity and the θ_H dependence of current-induced switching (see [Ref. 19]), which were well interpreted within the framework of SAHE. One may think the contribution of current-induced Oersted field (H_{Oe}) for switching. We calculated H_{Oe} at the switching current and H_{Oe} was estimated to be ~10 Oe at 1.8 mA, which is smaller than the coercivity of Py (~25 Oe) (see [Ref. 19]). Therefore, we consider that the SAH torque plays the major role for magnetization switching. In contrast to the orthogonal configuration, the switching behavior was not observed for the parallel configuration-device (see [Ref. 19]), again indicating negligible SHE and interface scattering effect. We conclude this is the first demonstration of SAHE-induced magnetization switching. In addition to the evaluation of linewidth modulation and the demonstration of switching, we examined the FMR lineshape analysis and the control experiment using the Cu | Py | Al-O device was done, which are given in [Ref. 19]. Those additional experiments support our conclusion of large SAHE in $L1_0$-FePt.

A great advantage for SAHE is the possibility of zero-field switching of perpendicular **m** by employing a SAHE polarizer with **p** tilted normal to the device plane. Since $L1_0$-FePt (111) with tilted magnetic anisotropy is exploited as a tilted polarizer [Ref. 26], we believe that $L1_0$-FePt showing large

SAHE becomes the key material to tackle the essential difficulty the spin orbit torque devices are confronted with.

References

[1]   M. I. Dyakonov and V. I. Perel, *Phys. Lett. A* **35**, 459-460 (1971).

[2]   J. E. Hirsch, *Phys. Rev. Lett.* **83**, 1834-1837 (1999).

[3]   Y. K. Kato, R. C. Myers, A. C. Gossard, and D. D. Awschalom, *Science* **306**, 1910-1913 (2004).

[4]   J. Wunderlich, B. Kaestner, J. Sinova, and T. Jungwirth, *Phys. Rev. Lett.* **94**, 047204 (2005).

[5]   A. Hoffman, *IEEE Trans. Magn.* **49**, 5172-5192 (2013).

[6]   B. F. Miao, S. Y. Huang, D. Qu, and C. L. Chein, *Phys. Rev. Lett.* **111**, 066602 (2013).

[7]   S. M.Wu, J. Hoffman, J. E. Pearson, and A. Bhattacharya, *Appl. Phys. Lett.* **105**, 092409 (2014).

[8]   T. Seki, K. Uchida, T. Kikkawa, Z. Qiu, E. Saitoh, and K. Takanashi, *Appl. Phys. Lett.* **107**, 092401 (2015).

[9]   T. Taniguchi, J. Grollier, and M. D. Stiles, *Phys. Rev. Applied* **3**, 044001 (2015).

[10] C. Qin, S. Chen, Y. Cai, F. Kandaz, and Y. Ji, *Phys. Rev. B* **96**, 134418 (2017).

[11] K. S. Das, W. Y. Schoemaker, B. J. van Wees, and I. J. Vera-Marun, *Phys. Rev. B* **96**, 220408(R) (2017).

[12] S. Iihama, T. Taniguchi, K. Yakushiji, A. Fukushima, Y. Shiota, S. Tsunegi, R. Hiramatsu, S. Yuasa, Y. Suzuki, and H. Kubota, *Nature electronics* **1**, 120-123 (2018).

[13] J. D. Gibbon, D. MacNeill, R. A. Buhrman, D. C. Ralph, *Phys. Rev. Applied* **9**, 064033 (2018).

[14] N. Nagaosa, J. Sinova, S. Onoda, A. H. MacDonald, and N. P. Ong, *Rev. Mod. Phys.* **82**, 1539-1592 (2010).

[15] D. Tian, Y. Li, D. Qu, S. Y. Huang, X. Jin, and C. L. Chien, *Phys. Rev. B* **94**, 020403(R) (2016).

[16] V. P. Amin, and M. S. Stiles, *Phys. Rev. B* **94**, 104419 (2016).

[17] S. C. Baek, V. P. Amin, Y. W. Oh, G. Go, S. J. Lee, G. H. Lee, K. J. Kim, M. D. Stiles, B. G. Park, and K. J. Lee, *Nature Mater.* **17**, 509-513 (2018).

[18] K. M. Seemann, Y. Mokrousov, A. Aziz, J. Miguel, F. Kronast, W. Kuch, M. G. Blamire, A. T. Hindmarch, B. J. Hickey, I. Souza, and C. H. Marrows, *Phys. Rev. Lett.* **104**, 076402 (2010).

[19] See Supplemental Materials at XXX.

[20] S. Mitani, K. Tsukamoto, T. Seki, T. Shima, and K. Takanashi, *IEEE Trans. Magn.* **41**, 2606-2608 (2005).

[21] I. M. Miron, K. Garello, G. Gaudin, P.-J. Zermatten, M. Costache, S. Auffret, S. Bandiera, B. Rodmacq, A. Schuhl, and P. Gambardella, *Nature* **476**, 189-193 (2011).

[22] L. Liu, C.-F. Pai, Y. Li, H. W. Tseng, D. C. Ralph, and R. A. Buhrman, *Science* **336**, 555-558 (2012).

[23] S. Fukami, T. Anekawa, C. Zhang, and H. Ohno, *Nature Nanotech.* **11**, 621-625 (2016).

[24] Y. Fan, P. Upadhyaya, X. Kou, M. Lang, S. Takei, Z. Wang, J. Tang, L. He, L.-T. Chang, M. Montazeri, G. Yu, W. Jiang, T. Nie, R. N. Schwartz, Y. Tserkovnyak, and K. L. Wang, *Nature Mater.* **13**, 699-704 (2014).

[25] N. H. D. Khang, Y. Ueda & P. N. Hai, *Nature Mater.* **17**, 808-813 (2018).

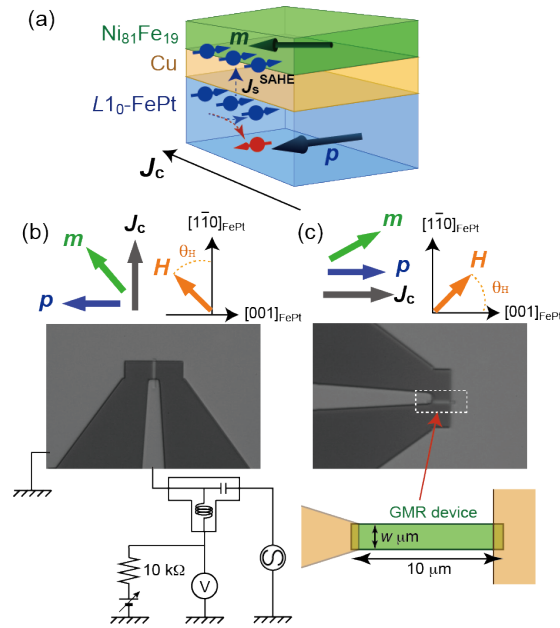[26] C. L. Zha, J. Persson, S. Bonetti, Y. Y. Fang, and J. Åkerman, *Appl. Phys. Lett.* **94**, 163108 (2009).

Figure 1 (a) Schematic illustration of SAHE in $L1_0$-FePt (30 nm) | Cu (3 nm) | Py (2 nm), where **p** and **m** are the unit vectors of $L1_0$-FePt and Py magnetizations, respectively. $\mathbf{J_c}$ denotes the charge current flow whereas $\mathbf{J_s^{SAHE}}$ denotes the spin current originating from SAHE. **(b)** Optical microscope images of devices for the orthogonal configuration and **(c)** the parallel configuration together with the relationship between **p**, **m**, $\mathbf{J_c}$, and external magnetic field ($\mathbf{H_{ext}}$). θ_H was defined to be the angle from $\mathbf{J_c}$. The setup for FMR measurement and the enlarged illustration of GMR device are also depicted.
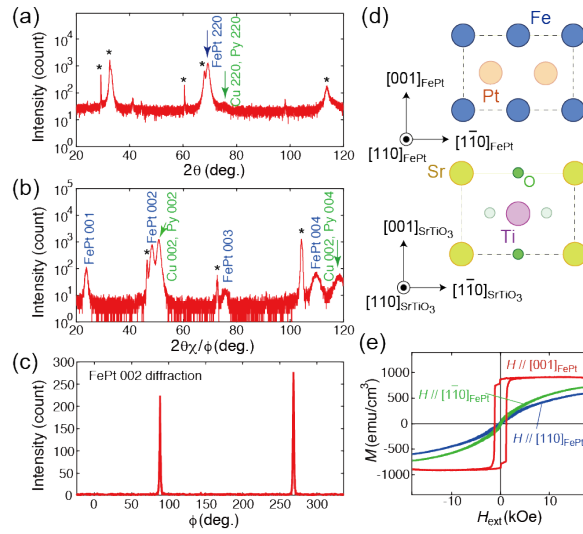
Figure 2 (a) Out-of-plane and **(b)** in-plane x-ray diffraction profiles for the $L1_0$-FePt (30 nm) | Cu (3 nm) | Py (2 nm) stack. The asterisks denote the reflections from the SrTiO$_3$ (110) substrate. **(c)** In-plane ϕ scan for FePt 200 diffraction. **(d)** Illustration of the epitaxial relationship between SrTiO$_3$ (110) and $L1_0$-FePt (110) planes. **(e)** Magnetization curves with H_{ext} applied along the in-plane [001] (red line) direction, the in-plane $[1\bar{1}0]$ direction (green line), and the out-of-plane [110] direction (blue line).
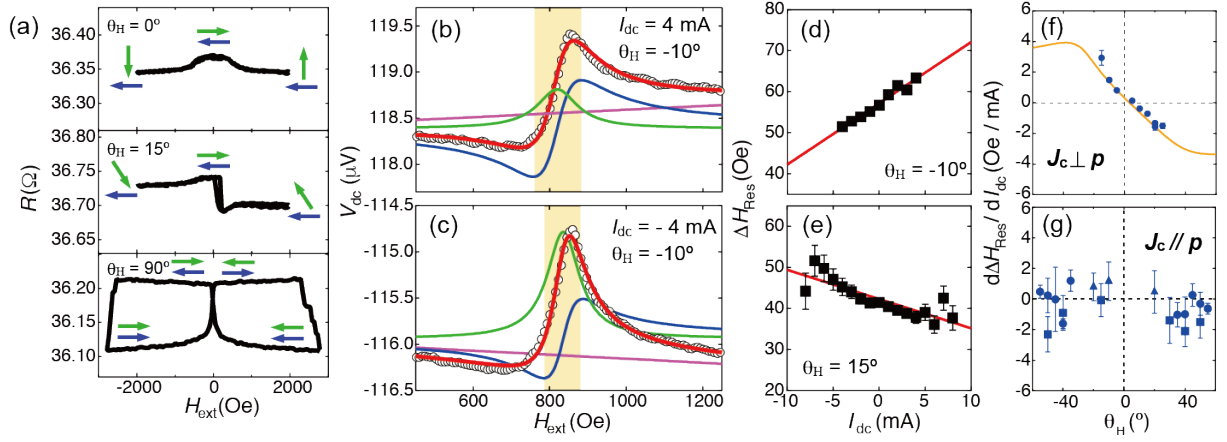
Figure 3 (a) Magnetoresistance curves for orthogonal configuration-device with $w = 4$ μm at $\theta_H = 0º$, 15º, and 90º. The blue and green arrows denote the $L1_0$-FePt and Py magnetizations, respectively. **(b)** FMR spectra for orthogonal configuration-device with $w = 4$ μm under the application of $I_{dc} = 4$ mA and **(c)** -4 mA. θ_H was set at -10º and f_0 was 4 GHz. The experimental data (black open circles) were fitted by the function (red curves) composed of lorentzian (green curves) and anti-lorentzian (blue curves) together with the linear background (purple lines). The orange-hatched areas are guides for eyes to see the linewidth modulation. **(d)** ΔH_{Res} versus I_{dc} for $\theta_H = -10º$ and **(e)** $+15º$ for orthogonal configuration-device. **(f)** $d\Delta H_{Res} / dI_{dc}$ as a function of θ_H for the orthogonal configuration- and **(g)** parallel configuration-devices. The solid curve in **(f)** represents the fitting result using Eq. 4. In **(g)**, different three devices (denoted by the solid circles, triangles and squares) were evaluated.
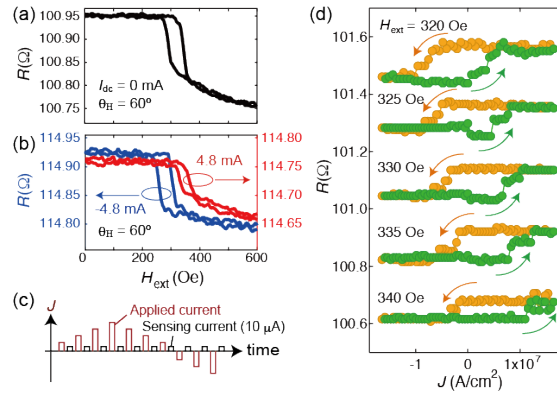
Figure 4 (a) Minor curves of CIP-GMR for orthogonal configuration-device with $w = 1$ μm at $\theta_H = 60°$ without applying I_{dc} and **(b)** with $I_{dc} = 4.8$ mA (red curve) and - 4.8mA (blue curve). **(c)** Measurement sequence for the switching experiment. First, "Applied current" was injected into the device, then R was measured by small "Sensing current" of 10 μA. **(d)** R as a function of applied current density (J) for orthogonal configuration-device measured at various H_{ext}. For clarity, the loops are shifted vertically. The arrows denote the current sweep directions.